# Optical birefringence in uniaxially compressed aerogels

**P Bhupathi**[1,4]**, L Jaworski**[1]**, J Hwang**[1,2]**, D B Tanner**[1]**,
S Obukhov**[1]**, Y Lee**[1,5] **and N Mulders**[3]

[1] Department of Physics, University of Florida, Gainesville, FL 32611-8440, USA

[2] Department of Physics, Pusan National University, Busan 609-735, Republic of Korea

[3] Department of Physics and Astronomy, University of Delaware, Newark, DE 19716, USA

E-mail: yoonslee@phys.ufl.edu

**Abstract.** The uniaxial strain dependence of refractive index anisotropy has been measured for a series of high-porosity aerogel samples. Uniaxial compression of compliant aerogels introduces an optical activity into the material. We report on the compression-dependent optical birefringence of samples with porosities from 95 to 99% under a uniaxial compression of up to 15% in the spectral range 320–800 nm.

[4] Present address: Department of Physics, Syracuse University, Syracuse, NY 13244, USA.

[5] Author to whom any correspondence should be addressed.

**IOP** Institute of Physics  **Φ** DEUTSCHE PHYSIKALISCHE GESELLSCHAFT

## Contents

## 1. Introduction

Highly porous and transparent silica aerogels were first synthesized in 1931 [1]. Manufactured by a sol–gel method [2, 3], aerogels are composed of a tenuous network of $SiO_2$ strands and can be synthesized in a wide range of porosities, especially in the high porosity limit, which extends up to 99.9% (only 0.1% silica). They are, in fact, the lightest solid materials with the lowest refractive index ever manufactured. Owing to their unique structure and high porosity, aerogels have found a wide variety of applications in science and technology [4]. Silica aerogels have been extensively used in Cerenkov counters in particle physics since the 1980s and have recently been utilized to capture cosmic dust in outer space [5, 6]. Their low thermal conductivity and high solar transmittance offer possibilities for use as superinsulating fillers for window systems and as a solar energy collector [7]. On a purely academic side, aerogels have also found a unique role as impurities or quenched disorder in systems such as liquid crystals [8] and quantum fluids, e.g. liquid $^4$He [9], $^3$He [10, 11] and their mixtures [12].

The influence of quenched disorder on unconventional superfluids and superconductors is of immense importance in the field of condensed matter physics and our motivation for this paper springs from our studies of superfluid $^3$He in aerogel. The aerogel strands, 3–5 nm in diameter, enclose open volumes or pores typically 30 nm wide, bringing the geometrical mean free path to a range of 100–150 nm at nominally 98% porosity. The coherence length in the superfluid $^3$He (the characteristic size of a Cooper pair: from 16 nm at 0 bar to 77 nm at 34 bar) is comparable to the mean free path provided by the aerogel structure, but is much larger than the aerogel strand diameter. Therefore, liquid $^3$He imbibed in high-porosity silica aerogel allows a systematic investigation of the effects of disorder on a p-wave spin-triplet superfluid. Various theoretical models for superfluid $^3$He in aerogel explain some—but not all—of the experimentally observed features of superfluid $^3$He in aerogel. In particular, there has been continuing interest in the consequences of the interaction between anisotropic disorder presented by aerogel and the anisotropic order parameter of superfluid $^3$He [13]–[16]. It has been proposed that this effect can be systematically studied by introducing controlled global anisotropy through uniaxial deformation of aerogel [16]. This scheme is attractive because

**IOP** Institute of Physics  $\Phi$ DEUTSCHE PHYSIKALISCHE GESELLSCHAFT

high-porosity aerogels possess an extremely low Young's modulus ($\approx 0.1$–$1$ MPa) and excellent mechanical compliance. Therefore, it is imperative to have a quantitative characterization of amount of anisotropy generated by compression or stretching for a systematic investigation.

Recently, Pollanen *et al* [17] demonstrated the presence of global anisotropy in compressed aerogels through optical birefringence. They measured the transmittance of white light passing through cylindrical aerogel samples under various degrees of compression between two crossed polarizers. However, no quantitative and spectroscopic information on birefringence was obtained. In this paper, we report the quantitative results of our optical characterizations of high-porosity aerogel samples subjected to a uniaxial strain of up to 15%. This work is an extension of our earlier publication [18] on 98% porosity aerogels. In this paper, we present more detailed measurements including the mechanical properties of aerogels with 95, 97, 98 and 99% porosities and a model for our results based on effective medium approximation (EMA).

## 2. Principle of measurement

The examination of a dielectric material placed between two crossed polarizers is a standard method of separating anisotropic materials from those that are isotropic. It is based on the fact that a linearly polarized light propagating through a uniaxially anisotropic medium experiences different indices of refraction for two rays with mutually orthogonal polarizations, namely, the ordinary ray (OR) and the extraordinary ray (ER). As a result, the light emerges from the medium with a phase difference $\delta$ between the two polarizations expressed by

$$\delta = \frac{2\pi d \Delta n}{\lambda}, \tag{1}$$

where $d$ is the thickness of the sample and $\lambda$ is the wavelength of light. $\Delta n$ represents the birefringence of the sample; it is defined as $\Delta n = n_e - n_o$, where $n_e$ and $n_o$ are, respectively, the indices of refraction corresponding to ER and OR. Equation (1) holds true when the angle of incidence of light is normal to the sample, which is the case for all our measurements.

Figure 1 shows a schematic diagram of our experimental setup. Suppose that the optic axis is along the compression axis, as indicated in figure 1. If a beam of intensity $I_o$ is incident on the sample, placed between two linear polarizers, the transmitted intensities for the crossed ($I_\perp$) and parallel ($I_\parallel$) orientations of the analyzer relative to the polarizer are given by [19]

$$I_\perp = I_o \sin(2\phi) \sin^2 \frac{\delta}{2}, \tag{2}$$

$$I_\parallel = I_o \sin(2\phi) \cos^2 \frac{\delta}{2}, \tag{3}$$

where $\phi$ is the angle between the polarization axis of the polarizer and the optic axis, fixed at $45°$ in our experiments. Here, we have neglected the absorption coefficients associated with the $n_e$ and $n_o$ directions. Equations (2) and (3) can be inverted to find the phase difference,

$$|\delta| = k\pi + 2\tan^{-1}\sqrt{\frac{I_\perp}{I_\parallel}}, \quad k = 0, 2, 4, \ldots, \tag{4}$$

$$|\delta| = (k+1)\pi - 2\tan^{-1}\sqrt{\frac{I_\perp}{I_\parallel}}, \quad k = 1, 3, 5, \ldots. \tag{5}$$
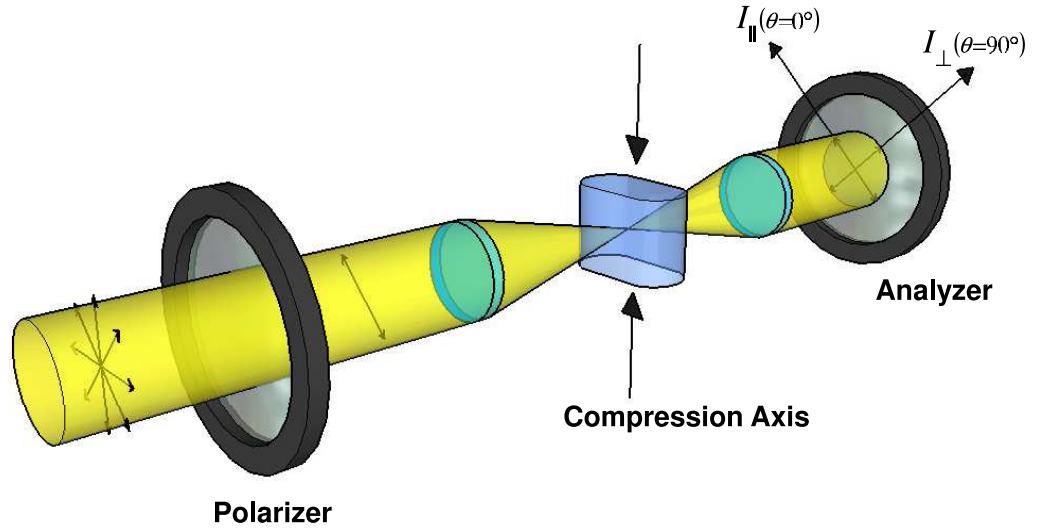
**Figure 1.** A visualization of the experimental setup. Collimated monochromatic light beam is passed through a polarizer with its polarizing axis fixed at 45° to the compression axis of the sample. The output intensity is measured through an analyzer at angle $\theta$ relative to the polarizer transmission axis.

By measuring the intensities $I_\perp$ and $I_\parallel$, one can extract the phase difference $\delta$ and hence $\Delta n$ from equation (1). Note that the above solutions only give the absolute value of $\Delta n$ but not the sign. The sign has to be inferred by other means, discussed later.

Because we are dealing with the uniaxial compression of the aerogel, we have to account for the increase in thickness ($d$) in the direction perpendicular to the compression by incorporating the Poisson ratio of the aerogel. If $d_o$ is the original thickness and $L$ is the length of the uncompressed aerogel, then for a small deformation ($\Delta L$), the thickness of the compressed aerogel is

$$d = d_o \left( 1 + \nu \frac{\Delta L}{L} \right), \tag{6}$$

where $\nu$ is the Poisson ratio of the aerogel. This modified thickness needs to be incorporated into equation (1) to extract $\Delta n$.

## 3. Experimental method

We adopted a technique similar to the one developed to investigate birefringence in liquid crystals [20] and polymers [21]. We have optically characterized three aerogel samples with 98% porosity (batch A), which will be referred to hereafter as samples 1–3. Another batch of aerogel samples with porosities ranging from 95 to 99% (batch B) have been used to measure their Poisson ratios and optical birefringence. The aerogels used in this study were made following the so-called two-step method first described by Tillotson and Hrubesh [2], using acetonitrile as the solvent to set the final aerogel density. The gels are typically aged for two weeks and then supercritically dried at 290 °C. The resulting aerogels are hydrophobic. The specific surface area, as determined from helium adsorption isotherms, is about $1000 \, \text{m}^2 \, \text{g}^{-1}$ with a primary particle diameter of 3 nm. The density of 98% aerogel is $0.044 \, \text{kg} \, \text{m}^{-3}$.
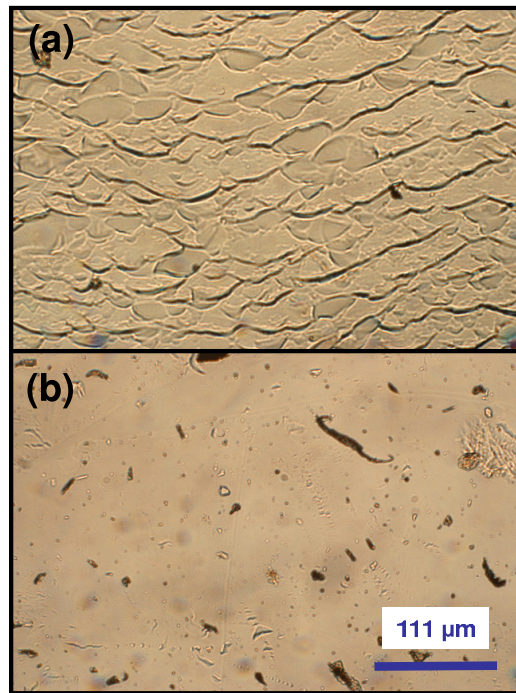
**Figure 2.** Images of the surfaces of the aerogel in white light. Cut surface in (a) and as-grown surface in (b).

The optical measurements were performed using a Zeiss MPM800 microspectrophoto-meter equipped with a Xe lamp as the light source and a photomultiplier tube as the detector. A platform was designed for mounting the aerogel between the polarizer and analyzer of the microscope, so that the light propagates in the direction perpendicular to the compression axis. The aerogel samples were synthesized in glass tubes in the shape of right circular cylinders. Two plane surfaces were cut parallel to the cylinder axis on either side of the cylinder using a high-speed diamond cutter. This process provided two parallel and flat surfaces for optical measure-ments, eliminating tilt of the beam at the surface of the aerogel. The cut and as-grown surfaces of an aerogel sample were imaged using a white light and pictures of those images are shown in figures 2(a) and (b). At the scale observed, the pictures suggest that the as-grown surface of the aerogel is much smoother than the machine-cut aerogel. This could be of importance to trans-verse acoustic impedance measurements of superfluid $^3$He in aerogel, where the contact between the aerogel and the transducer surfaces is crucial in observing the superfluid transition features. The polarized light beam ($\approx 0.5 \times 0.3 \, \text{mm}^2$) was focused on the sample with a focusing lens and the output light was viewed through a $10\times$ objective lens located before the analyzer (figure 1). The aerogel samples were compressed along the cylindrical axis and the strain was determined using a micrometer vise with a non-rotating spindle. For each compression–decompression cycle, the wavelength was scanned from 320 to 800 nm in 4 nm increments and the output intensity of light was measured for various angles of $\theta$, the angle of the analyzer relative to the polarizer transmission axis that was always fixed at $45°$ to the compression axis. Strong absorp-tion by the optical components limited the short-wavelength measurements to approximately 320 nm and the photomultiplier cutoff dictated the 800 nm long-wavelength limit.
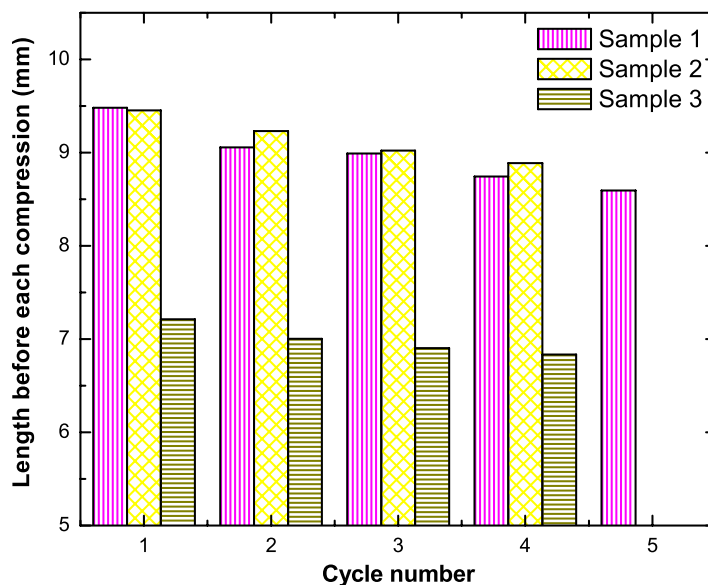
**IOP** Institute of Physics Φ DEUTSCHE PHYSIKALISCHE GESELLSCHAFT



**Figure 3.** Graph showing shrinkage of aerogels (batch A) after every cycle of compression and decompression. The bars in the graph denote the length measured before each cycle to 15% compression. Each compression–decompression cycle typically took about 4 h. No significant relaxation in the length was observed after the completion of each cycle.

## 4. Results and discussion

### 4.1. Mechanical properties

Before we discuss the birefringence, we would like to briefly describe some mechanical effects of compressive strain on the aerogel. It is known that compression can lead to a reduction in the elastic modulus of high-porosity aerogels [22, 23], and shrinkage or damage can occur in aerogels during the supercritical drying stages of the gel [17, 24, 25] or during capillary condensation [26]. In our measurements we observed a substantial amount of shrinkage in length along the compression axis for the aerogel samples that underwent cycles of compression and decompression. In figure 3 the length of the aerogel before each cycle of compression up to 15% is plotted for three samples of batch A. In general, the shrinkage is found to be the largest after the first compression–decompression cycle and decreases for the subsequent cycles. After the completion of four cycles, the total amount of shrinkage was 9, 7.5 and 6.7% for samples 1–3, respectively. However, no shrinkage was observed for the samples cycled up to 5% compression. Our observation is consistent with the elastic measurements of Gross *et al* [22], in which most samples recovered 99.5% or better of their original length after compressions of a few per cent, although we have to point out that their sample preparation method was different from ours.

### 4.2. Poisson ratio measurements

To our knowledge, the only known measurements of the Poisson ratio of high-porosity aerogels in the literature are from Gross *et al* [23, 26] and Pollanen *et al* [17]. Gross *et al* determined
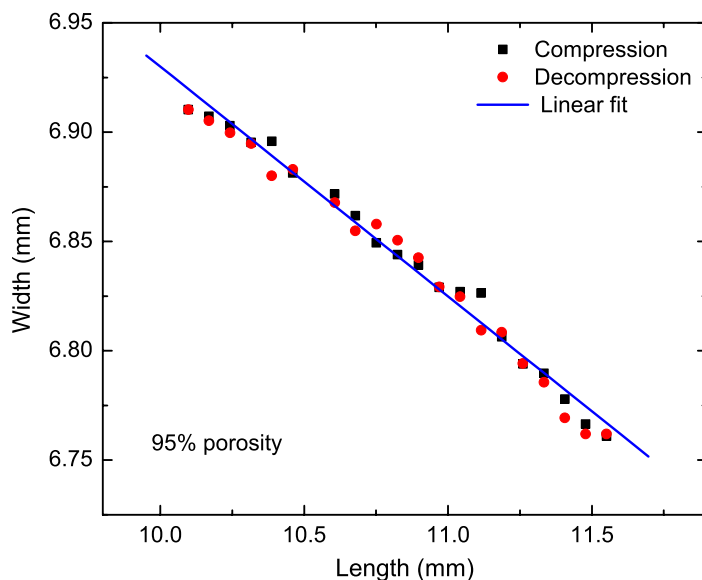
**Figure 4.** The width versus length of an aerogel sample with 95% porosity undergoing a compression of up to 15%. The black squares (red circles) were taken on compression (decompression). The solid line is a linear fit to the data.

**Table 1.** Poisson ratios of aerogel samples of different porosities.

| Porosity (%) | Poisson ratio ($\nu$) |
|---|---|
| 95 | $0.112 \pm 0.003$ |
| 97 | $0.094 \pm 0.002$ |
| 98 | $0.147 \pm 0.005$ |
| 99 | $0.143 \pm 0.005$ |

the Poisson ratio from the longitudinal and transverse sound velocity in the aerogel and found $\nu \approx 0.2$, independent of porosity, whereas Pollanen *et al* determined $\nu \approx 0.3 \pm 0.05$ based on their optical images. We measured the Poisson ratio by direct mechanical compression using the same micrometer vise used in our birefringence measurement. We believe that this method is more appropriate for determining the actual change in $d$ caused by uniaxial compression. The samples were cut as described in section 3 and were compressed in a micrometer vise mounted on a $x$–$y$ micro positioning stage under a microscope. The compression in the $x$-direction was varied from 0 to 15% determined by the micrometer reading. The change in width of the sample (in the $y$-direction) was measured using the $x$–$y$ micro positioning device with the help of the eyepiece cross-hairs. A laser beam threading through the sample in the $y$-direction was used to clearly identify the aerogel boundary. A typical plot of the width versus the length of a 95% porosity sample is shown in figure 4. The slope of a straight line fit (solid line in figure 4) to the data yields the Poisson ratio. Measurements were repeated on different samples with the same porosity and the average Poisson ratio was calculated. The average Poisson ratios for different porosity samples are given in table 1 and are used in our analyses. Our values fall lower than 0.2, between 0.1 and 0.15 for porosities from 95 to 99%. The difference might be caused by
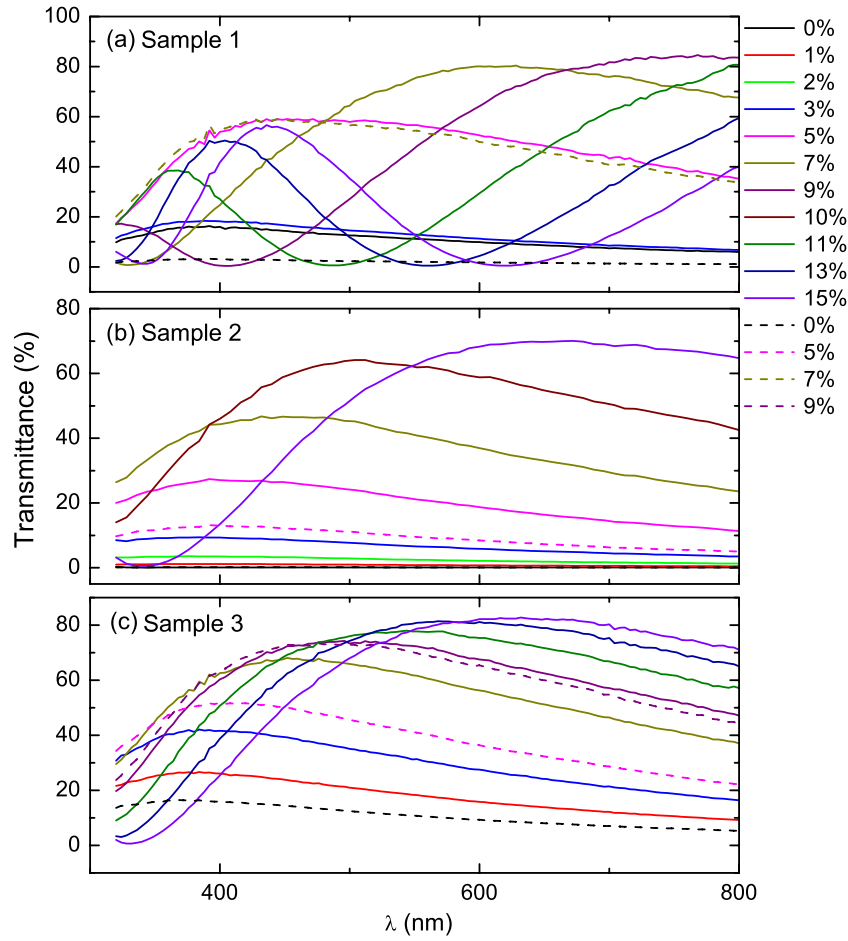
**Figure 5.** The transmittance (the ratio as defined in section 4.3) of samples 1–3 (a–c, respectively) in the crossed-polarizer configuration as a function of wavelength. The solid (dashed) lines are data taken on compression (decompression).

a small nonlinearity evident in figure 4 because the Poisson ratio determined from the sound velocity is presumably in the low strain limit.

## 4.3. Optical transmission measurements

Figure 5 displays the transmittance of samples 1–3 in the crossed-polarizer configuration ($\theta = 90°$) as a function of wavelength on the fourth compression–decompression cycle. The transmittance was determined as the ratio of the transmitted intensity to a background intensity measured without a sample but with the two polarizers aligned parallel ($\theta = 0°$). The traces taken on compression (decompression) are represented by the solid (dashed) lines. In this configuration, any finite transmittance indicates the presence of optical activity in the aerogel. At zero compression, the transmittance is very low, because it is the transmittance of a nearly isotropic substance between crossed polarizers. With increasing compression there is initially an increase in transmittance across the spectrum and then an oscillatory behavior, both with wavelength at a given compression and with compression at a given wavelength. For sample 1
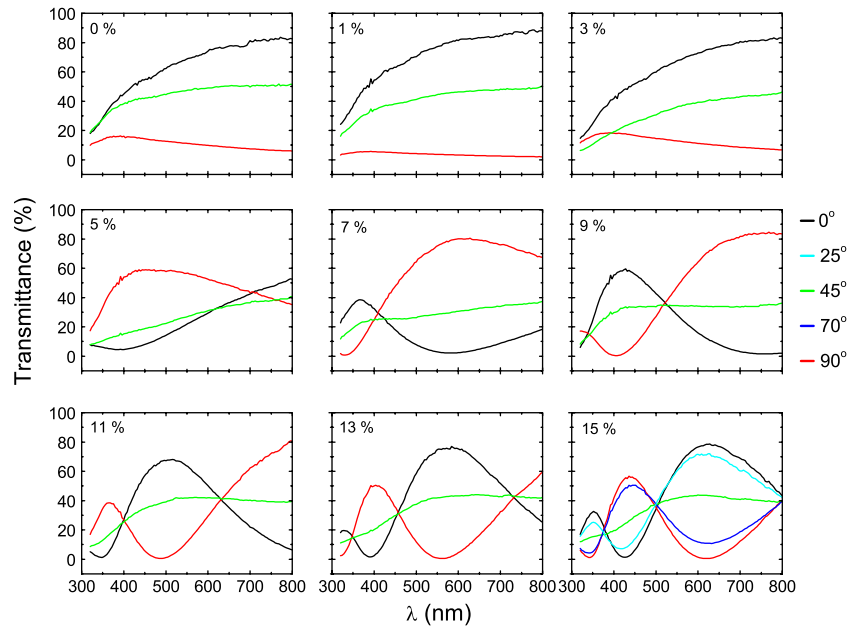
**Figure 6.** Transmittance versus wavelength of sample 1, with progressively increasing compression shown in panels going from left to right (0–15%), at different angles of the analyzer (see the legend on the right).

in figure 5(a), the transmittance reaches a broad maximum by 7% compression. The position of the maximum moves progressively towards longer wavelengths for higher compression and then a second maximum emerges from the short wavelength side. These oscillations are caused by the birefringence. For a given compression, the path length $d$ and refractive index anisotropy $\Delta n$ are fixed; however, the phase difference $\delta$ increases with decreasing wavelength, and the transmittance, in accord with equation (2), swings between the maximum transmittance and zero. One other factor, scattering of light in the aerogel, affects the spectra. Because the sizes of the aerogel strands are much smaller than the wavelength of light, Rayleigh scattering is responsible for the increasing envelope of the transmittance between 320 and 800 nm. Similar behavior has previously been observed in aerogels with comparable porosities [27].

We note that sample 1 shows non-zero transmittance in the uncompressed state. The transmittance first decreases with compression and then starts to increase after 2% compression. We believe that this behavior is due to the inherent anisotropy in the aerogel sample, probably from the growth process or through the repeated compressions [17]. Our results also exhibit substantial hysteresis between the compression and decompression. For example, the transmittance for 7% in sample 1 on decompression actually matches that for 5% on compression, as shown in figure 5(a). This result can be understood by taking into account the shrinkage in the length of the aerogel ($\approx 2\%$) occurring during the fourth cycle, as can be inferred from figure 3. The built-in anisotropy is also manifest in sample 3, as can be seen in figure 5(c).

Figures 6–8 display the transmittance for different angles of the analyzer for samples 1–3, respectively. The panels show data at progressively increasing compression, from 0 (top left) to 15% (bottom right). In an uncompressed aerogel, the effect of optical birefringence is modest due to the weak built-in anisotropy mentioned above (samples 1 and 3). Therefore, the polarization-angle dependence of the transmittance is easily understood. When compressed
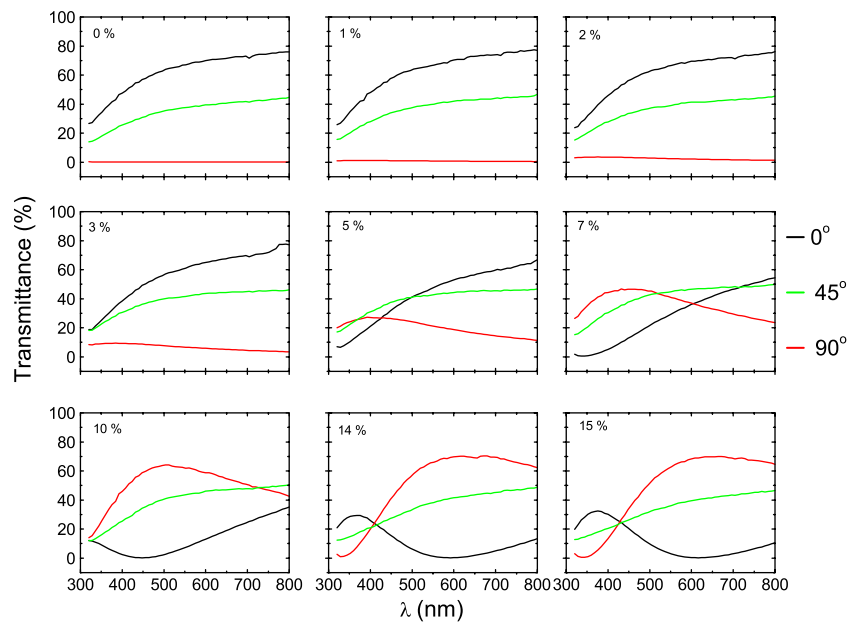
**Figure 7.** Transmittance versus wavelength of sample 2 with increasing compression shown in panels going from left to right (0–15%) at different angles of the analyzer.
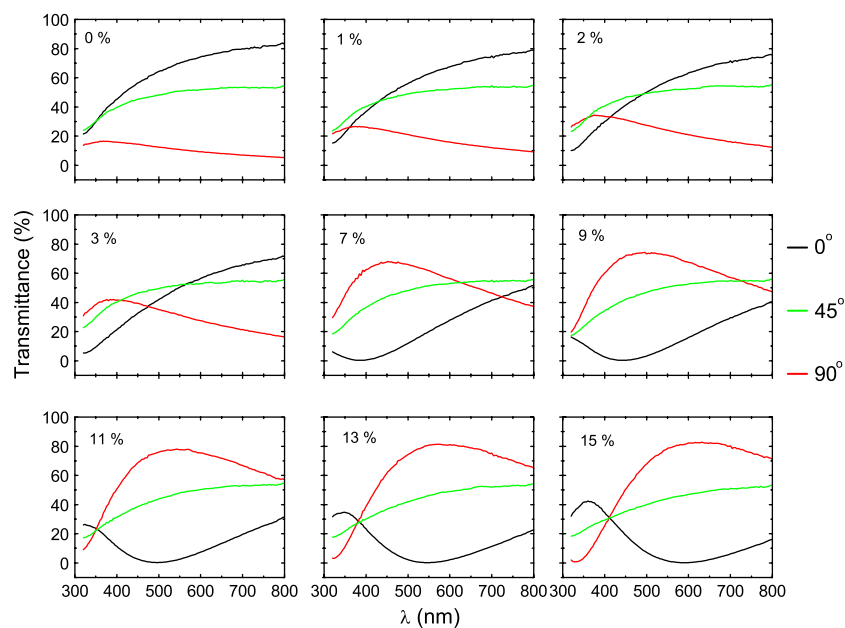
**Figure 8.** Transmittance versus wavelength of sample 3 with increasing compression shown in panels from left to right (0–15%). The legend on the right shows the different angles of the analyzer.

by 15%, the birefringence produces oscillatory behavior as the phase difference $\delta$ is inversely proportional to the wavelength. One particular feature of this observation is the appearance of the nodes at which the transmittance becomes independent of the angle of the analyzer.

At these nodes the emerging light is circularly polarized, with the phase difference between OR and ER being an odd integer multiple of $\pi/2$. For example, the 15% compressed aerogel (sample 1) behaves as a quarter-wave plate at the wavelengths of the nodes near 375, 500, and 800 nm (see figure 6), which is periodic in frequency, in accordance with the birefringence in the compressed aerogel. It is worth mentioning that compressed aerogels have the potential to serve as tunable wave plates, with some advantages over conventional tunable waveplates such as Babinet compensators, including smaller reflectance, absence of gradient effect and no limitation on the beam size.

In order to understand fully our results, we need to consider the effects of birefringence associated with anisotropy, Rayleigh scattering and dispersion. Therefore, the expression for transmittance in the crossed-polarizer configuration should be modified from equation (2) to

$$T = A \exp\left(\frac{-B}{\lambda^4}\right) \sin(2\phi) \sin^2 \frac{\pi d \Delta n}{\lambda}. \tag{7}$$

The first exponential term accounts for the Rayleigh scattering. The dispersion effect is incorporated in $\Delta n$ by a simplified form of the Sellmeier dispersion equation called the Cauchy formula [19]:

$$\Delta n = C + \frac{D}{\lambda^2}. \tag{8}$$

The Sellmeier form has been previously used in the literature to fit the birefringence dispersion in glasses and liquid crystalline materials [21, 28, 29]. The light path length is also corrected by equation (6), using the reported value of the Poisson ratios $\nu = 0.2$ [23, 26] (the Poisson ratios of these samples were not measured in this work). The above two equations are used to fit our transmittance for all samples at 15% compression by a nonlinear least square fitting method, with $A$, $B$, $C$ and $D$ as our fitting parameters [18]. The results are shown in figure 9(a) [18] as solid lines. In figure 9(b) we plot the $\Delta n(\lambda)$ directly obtained from our measurements of $I_\perp/I_\parallel$ using equations (1), (4) and (5). For example, the three red traces represent the birefringence for sample 1, assuming three different branches of $k$ in equations (4) and (5). In each trace only the nearly horizontal portions are meaningful and the conjoined traces of the horizontal sections correctly reflect the birefringence of the sample. Also displayed in the plot is $\Delta n(\lambda)$, calculated using equation (8) and $C$ and $D$ obtained from the fit. They are in excellent agreement with each other.

Adopting the same fitting procedure, we find very good agreement with the measured $\Delta n(\lambda)$ at all compressions. These results are shown for sample 3 in figure 10 for strains between 2 and 13% over the whole wavelength range. Figure 11(a) shows the strain dependence of the optical birefringence for the three samples with 98% porosity. All samples studied follow a quasi-linear dependence with a weak nonlinearity. The built-in anisotropy is manifest in this plot for samples 1 and 3. We can only determine the absolute value of birefringence through our measurements. Therefore, it is reasonable to think that the birefringence of sample 1 actually changes its sign around the 3% strain point, suggesting that the small uniaxial compression compensates, in effect, the built-in anisotropy in the sample. In contrast, the built-in anisotropy in sample 3 is in the same direction caused by uniaxial compression. $\Delta n$ for all compression cycles of sample 3 is shown in figure 11(b). In each cycle the strain was determined based on the sample length at the beginning of each cycle. $\Delta n$ shifts up with the number of cycles and seems to saturate at the fourth cycle of compression. However, the overall change in $\Delta n$ for a given strain range remains almost the same.
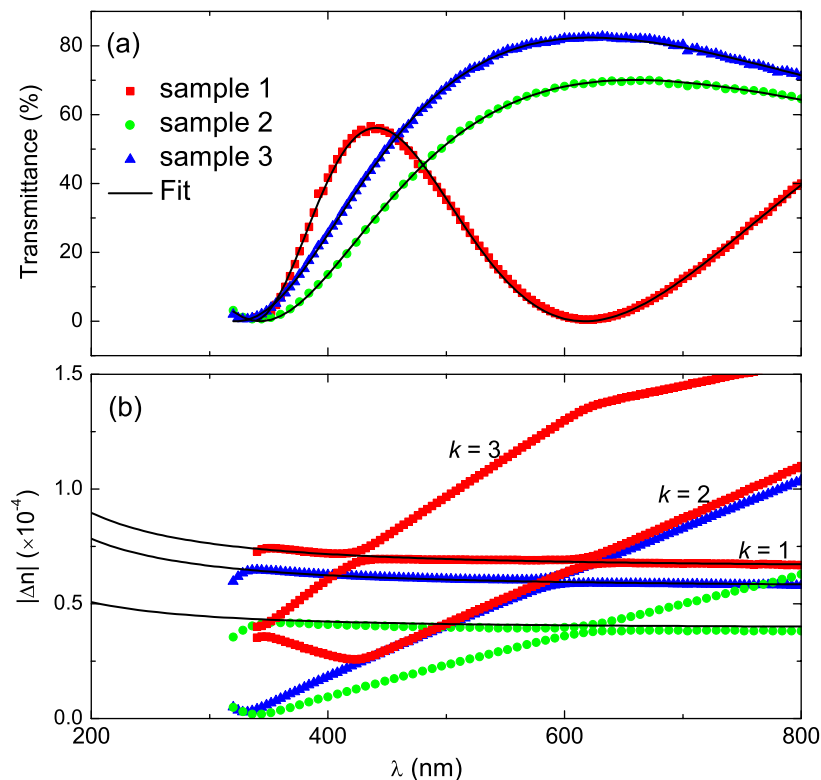
**Figure 9.** Transmittance and birefringence data in the cross-polarized setup for samples 1–3 at 15% compression. The solid lines in both panels are the results of the fit as explained in the text.
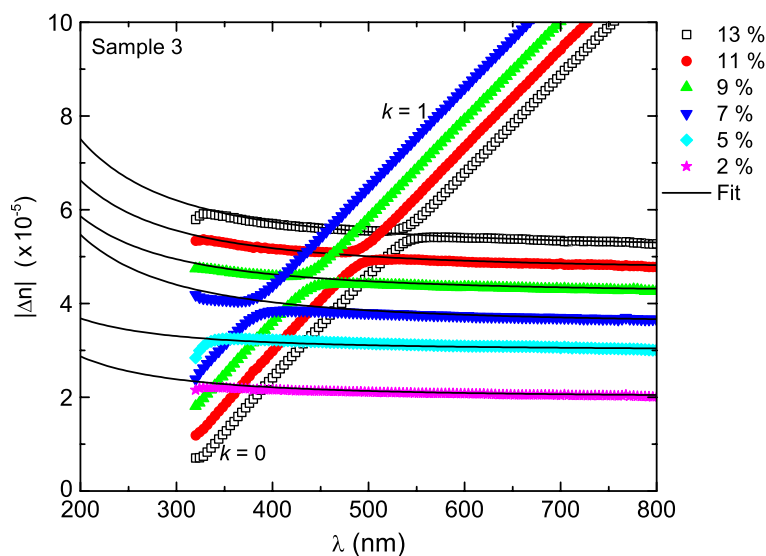
**Figure 10.** Birefringence dispersion in aerogel sample 3 for various strains (see the legend) ranging from 2 to 13%. The black lines are the $\Delta n$ calculated by fitting the wavelength-dependent transmittance data using equations (7) and (8).
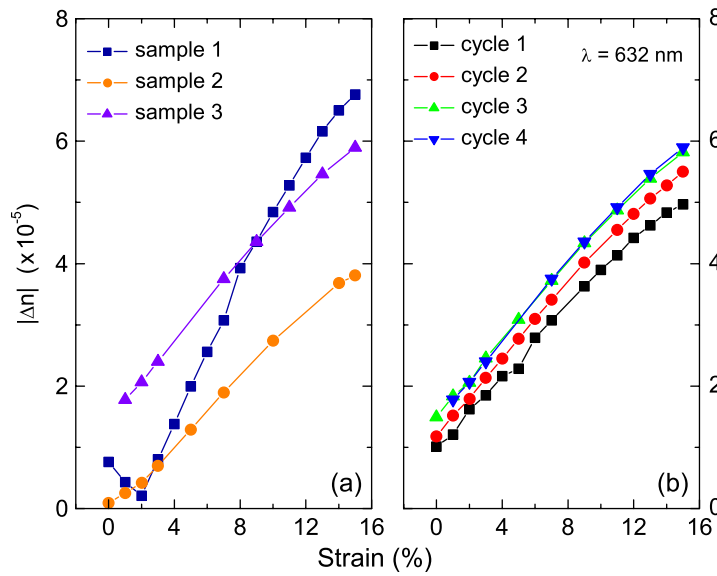
**Figure 11.** (a) $\Delta n$ versus strain at 632 nm for samples 1–3 on their fourth cycle of compression. (b) $\Delta n$ versus strain at 632 nm for sample 3 at different cycles of compression from its virgin condition (cycle 1).
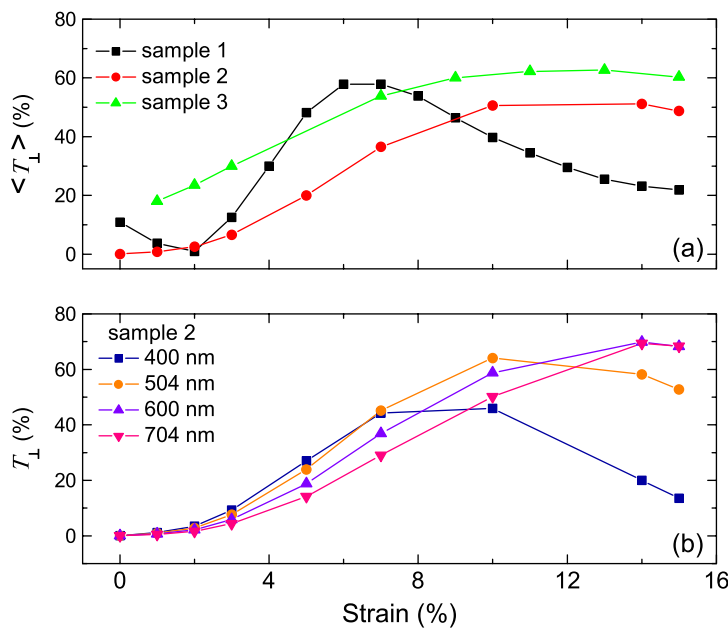


**Figure 12.** (a) Total transmittance ($\langle T_\perp \rangle$) in the cross-polarized configuration integrated for all wavelengths (320–800 nm) as a function of strain for all samples. (b) The transmittance ($T_\perp$) of sample 2 between the crossed polarizers for several wavelengths.

Figure 12(a) illustrates the total transmittance ($\langle T_\perp \rangle$) of the three samples integrated over the whole wavelength range as a function of applied strain. The transmittance for samples 2 and 3 rises initially and starts to drop beyond 10%. Sample 1 behaves a little differently,
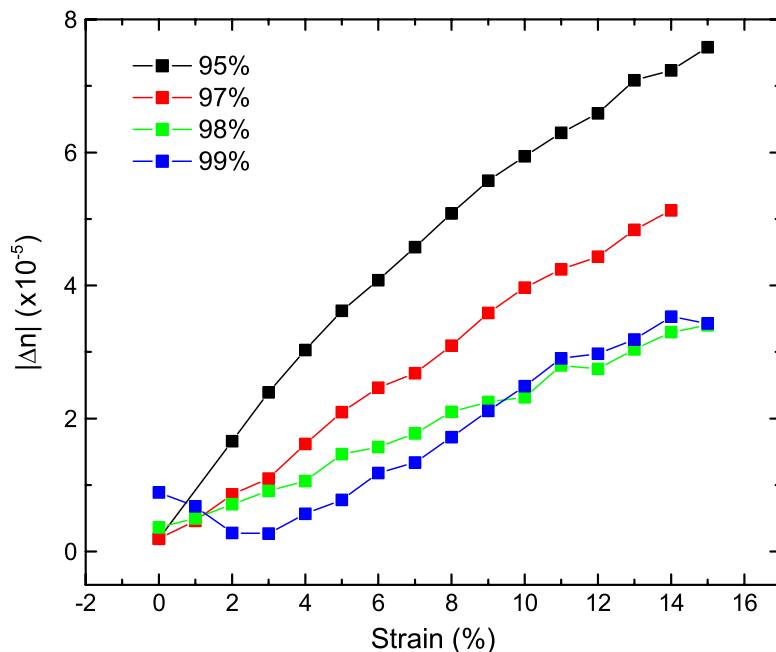
**Figure 13.** Strain dependence of birefringence for aerogel samples (batch B) with various porosities.

with a more pronounced oscillatory behavior. As explained previously in the discussion of figures 6–8, the transmittance is expected to oscillate since the aerogel placed between the crossed polarizers acts just like a waveplate tunable with the compressive strain. Our results are in contrast to the recent observation by Pollanen *et al* [17]. They performed a similar measurement with a 98% cylindrical aerogel sample ($\approx 8$ mm diameter) between two crossed polarizers. Their transmittance (using white light) showed a linear strain dependence to their highest uniaxial compression at 20% and was uniform throughout the sample. In this case, one effectively measures the average intensity of light traversing different path lengths throughout the cylindrical sample. Figure 12(b) plots the wavelength-dependent transmittance ($T_\perp$) of sample 2, which conforms to the waveplate character of the compressed aerogel, where the maximum in the transmittance occurs at different compressions induced at different wavelengths. A similar behavior was observed for samples with porosities other than 98%. Figure 13 depicts the optical birefringence as a function of strain on samples with porosities of 95, 97, 98 and 99% (batch B). In evaluating the birefringence our measured Poisson ratio values, as determined in the previous section, were used. The data shown in figure 13 were obtained during the second compression-decompression cycle. As seen from the figure, the birefringence for the various porosities is of comparable magnitude and the 99% aerogel sample also shows built-in anisotropy almost identical to that of sample 1.

## 4.4. Effective medium model

In this section, we develop a simple model for our results in an attempt to correlate the birefringence with the structural changes. The optical properties of the aerogel can be modeled by the well-known EMAs [30, 31], the Bruggemann EMA or the Maxwell Garnett theory

(MGT). These approaches are applicable here because the wavelength of the light used is much longer than the inter-strand distance. The effective dielectric function of the composite medium is calculated by averaging the dielectric permittivities of its constituents, namely air and $SiO_2$ grains with their respective volume fractions. In the case of compressed aerogels, the dielectric function is a tensor due to the anisotropy generated and the depolarization effects become important. Note that there are no absorption bands in the aerogel for the measured wavelength range, so that the refractive index can be simply calculated by setting $n = \sqrt{\varepsilon}$.

In the Bruggeman model, considering the aerogel as a collection of uniformly distributed needle-shaped $SiO_2$ pieces, the dielectric constant $\varepsilon_B$ is formulated as

$$f \frac{\varepsilon_{SiO_2} - \varepsilon_B}{g\varepsilon_{SiO_2} + (1-g)\varepsilon_B} + (1-f)\frac{\varepsilon_{air} - \varepsilon_B}{g\varepsilon_{air} + (1-g)\varepsilon_B} = 0, \tag{9}$$

where $f$ is the filling fraction of $SiO_2$, $\varepsilon_{SiO_2} = 2.34$ and $\varepsilon_{air} = 1.00$. $g$ is the depolarization factor, related to the topology of the inclusion material and the orientation of the applied electric field. For the cylindrical axis parallel and perpendicular to the electric field, $g_\parallel = 0$ and $g_\perp = 1/2$, respectively. With $f = 0.02$ (98% porosity), the indices of refraction for two perfectly aligned cases are evaluated as $n_o = 1.0133$ for the ordinary component ($g_\parallel = 0$) and $n_e = 1.0081$ for the extraordinary component ($g_\perp = 1/2$). This sets the upper bound of birefringence for this model $\Delta n = n_e - n_o \approx -5 \times 10^{-3}$, a reasonable result considering that our birefringence at 15% is $\sim 5 \times 10^{-5}$. The index of refraction for an isotropic aerogel can be estimated to be $n = (1/3)n_o + (2/3)n_e \approx 1.010$, in good agreement with the previously reported values [32].

In the MGT, we model the system as a collection of $SiO_2$ ellipsoids embedded in air with the respective dielectric permittivities. The procedure discussed here has been successfully applied before in understanding the form birefringence of porous semiconductors and dielectrics [33, 34]. The MGT dielectric function for oriented ellipsoids [31] is given by

$$\varepsilon_{\perp,\parallel}^G = \varepsilon_{air} + \varepsilon_{air} \frac{f(\varepsilon_{SiO_2} - \varepsilon_{air})}{g_{\perp,\parallel}(1-f)(\varepsilon_{SiO_2} - \varepsilon_{air}) + \varepsilon_{air}}. \tag{10}$$

The spectral dispersion of the refractive index of $SiO_2$ in the above equation is given by a three-term Sellmeier form given by Malitson [28]:

$$n_{SiO_2}^2(\lambda) = 1 + \sum_i \frac{A_i \lambda^2}{\lambda^2 - \lambda_i^2}, \tag{11}$$

where for $i = 1, 2, 3$, $A_i$ and $\lambda_i$ are the constant fit parameter values determined from the experimentally measured values of the refractive index of $SiO_2$ (see [28]). The constants $g_\parallel$ and $g_\perp$ appearing in equation (10) are the geometrical depolarization factors similarly defined as in the Bruggemann model [35], corresponding to the electric field being parallal or perpendicular to the principal axes of the ellipsoid. Their values depend on the ratios of the polar to the equatorial axes of an ellipsoid. Tabulated values of $g$ can be found in the literature [36]. For example, a plane has $g_\parallel = 1$, $g_\perp = 0$, an infinite cylinder has $g_\parallel = 0$, $g_\perp = 0.5$ and a sphere has $g_\parallel = g_\perp = 0.333$. If the ellipsoid is a spheroid where two of the principal values of $g$ are equal, we have the condition $g_\parallel + 2g_\perp = 1$. Using $g_\parallel$ as the fitting parameter, the birefringence $n_e - n_o = \sqrt{\varepsilon_\parallel} - \sqrt{\varepsilon_\perp}$ is calculated using equation (10), which also gives a negative sign to our birefringence values. This is compared against our measured values of birefringence in
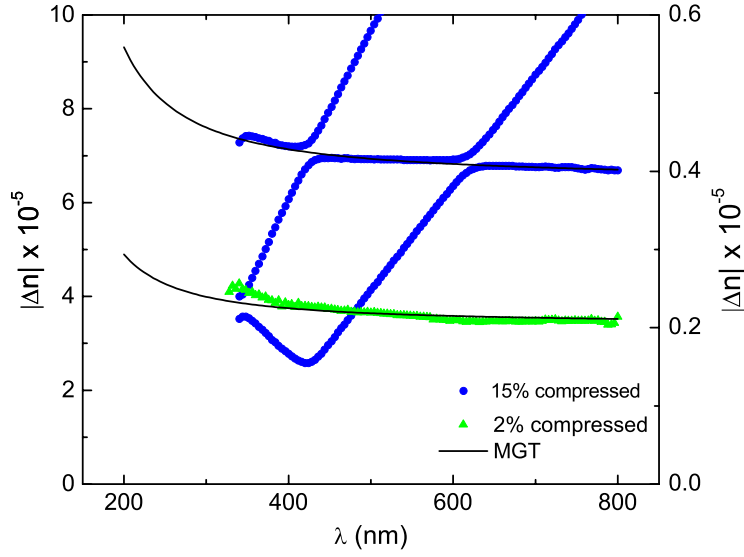
**Figure 14.** Measured birefringence values of sample 1 at 15% compression (circles) on the left $y$-axis and 2% compression (triangles) on the right $y$-axis. Solid black lines are from the MGT equation (10), with $g_\parallel = 0.340$ for 15% compressed aerogel and $g_\parallel = 0.333$ for 2% compressed aerogel.

figure 14. The bottom trace of the figure shows the birefringence of sample 1 at 2% compression and the top trace at 15% compression. The best fits to our experimental data yield values of $g_\parallel = 0.340$ for 15% compressed aerogel and 0.333 for 2% compressed aerogel, indicating that at 2% compression, the aerogel particles maintain a spherical shape, and when compressed by 15% they deviate towards a spheroid by about 3% in length. Both models predict $\Delta n \propto f$, which is in qualitative agreement with our results (see figure 13).

When the needle-shaped aerogel strands are not perfectly aligned the birefringence can be expected to be lower than the perfectly aligned case. The degree of misalignment can be described by the Hermans orientation function $\chi(\theta)$ [37], such that

$$\Delta n = \Delta n_{\text{max}} \chi(\theta), \tag{12}$$

where $\chi(\theta)$ is given by $\frac{1}{2}(3\langle\cos^2\theta\rangle - 1)$ and $\Delta n_{\text{max}}$ is the maximum birefringence for the case of perfect alignment. $\langle\cos^2\theta\rangle$ is the average over polar angle $\theta$ between the optic axis and the needle direction. This quantity is $1/3$ for an isotropic configuration. There are various theoretical models in polymer physics that describe the molecular orientation through uniaxial deformation and one can derive the appropriate form of the Hermans function for the system under study. In our case, assuming a linear deformation of the aerogel needle about the network of joints, the $\langle\cos^2\theta\rangle$ can be given as

$$\langle\cos^2\theta\rangle = \frac{1}{3}\left(1 - \frac{\Delta L}{L}\right)^2. \tag{13}$$

This relation is derived in the appendix. Using equations (12) and (13) and the value of $\Delta n_{\text{max}} = n_{\text{e}} - n_{\text{o}} \approx -5 \times 10^{-3}$ from our previous consideration, $|\Delta n|$ is plotted in figure 15 as a function of strain along with our experimentally measured values for samples 1–3. As seen in this figure, as well as in figures 11 and 13, the measured $\Delta n$ show a small curvature, indicating
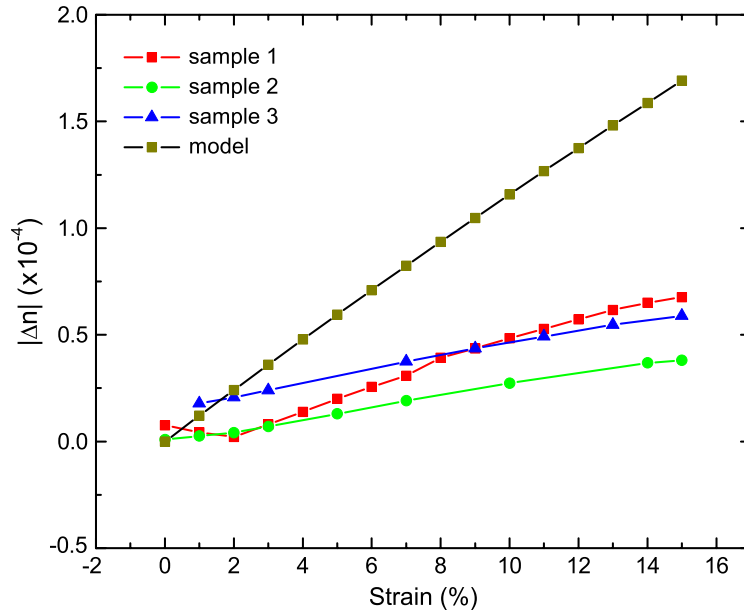
**Figure 15.** Strain dependence of birefringence for aerogel samples 1–3 and calculated values using the Hermans orientation function.

the presence of a small quadratic strain dependence with a negative coefficient. This behavior is consistent with equation (13) ($\Delta n < 0$). However, the magnitude of optical birefringence is about 1/3 of the value predicted by this model. Here, we should note that the magnitude of $\Delta n_{max}$ is estimated in a model of ideal needle-like cylinders made of $SiO_2$. It is also assumed that all the needles would rotate in response to uniaxial compression. This idealization is far from the actual structure of the aerogel strand, which is formed by random cluster–cluster aggregation of nanometer-scale aerogel particles [38, 39]. In a real aerogel, there are many dead-end clusters attached to the backbone structure at one end and with the other end dangling [39]. These dead-end clusters neither contribute to the mechanical strength of the material nor generate rotation to the first order in response to uniaxial strain [40]. A more sophisticated model should also incorporate local variations of cluster orientation ($\widehat{n}_{loc}$) in a strand whose orientation is represented by $\widehat{n}_{st}$ (see figure 16). For a random structure, $\widehat{n}_{st}$ and $\widehat{n}_{loc}$ are correlated and are characterized by the correlation function $\kappa = \frac{3}{2}(\widehat{n}_{st} \cdot \widehat{n}_{loc})^2 - \frac{1}{2}$. Therefore, this correlation effect should be included as a prefactor in equation (13). The value of $\kappa$ depends on the detailed structure of the aerogel but should be $0 < \kappa < 1$. Based on our measurements, we find that $\kappa \approx \frac{1}{3}$ (assuming no dead clusters), which limits the variation of $\widehat{n}_{loc}$ within $\approx 60°$ with respect to $\widehat{n}_{st}$.

## 5. Summary

We have measured the birefringence of uniaxially compressed high-porosity aerogels in the visible range of the spectrum. A mechanical compression beyond 5% on the aerogel shows hysteresis in transmittance data, which can be correlated to the non-recovery of the aerogel to its uncompressed length. The birefringence exhibits quasi-linear dependence on the compression and is large enough to observe the wave plate phenomenon. The birefringence, and its
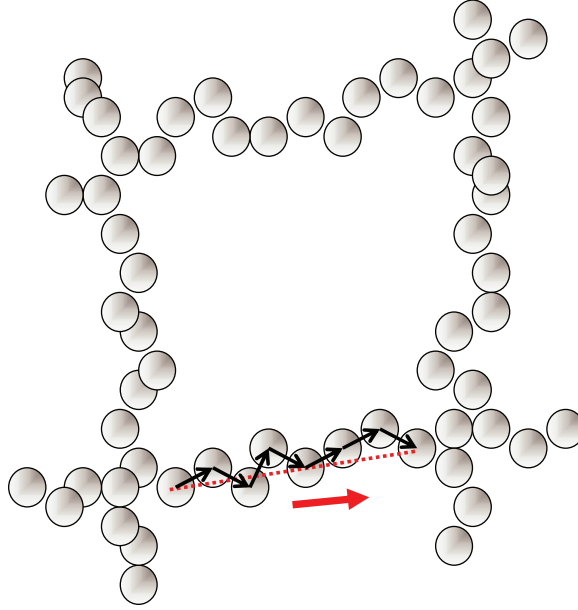
**Figure 16.** A cartoon of the aerogel structure depicting local variations of cluster orientation of a strand. The thick red arrow represents $\widehat{n}_{st}$ and the small black arrows indicate the direction of local cluster orientation, $\widehat{n}_{loc}$.

dispersion, is in excellent agreement with the Sellmeier oscillator model. The effective medium approximation model provides a satisfactory picture of the observed phenomena.

## Acknowledgments

## Appendix

Here, we derive equation (13) relating the Hermans anisotropy function to mechanical strain. Let $L$ be the initial length of the uncompressed aerogel and $\Delta L$ be the change in length after compression. Define the compression or stretch ratio as

$$\alpha = \ln \frac{L}{L_{min}}, \tag{A.1}$$

where $L_{min} = L - \Delta L$, so that in the uncompressed state $\alpha = 0$ and $\alpha > 0$ when compressed. We consider an aerogel strand of length $\ell$ initially making an angle $\theta$ with respect to the $\hat{z}$-axis. After a small deformation by an angle $\delta\theta$, the change in length along the $\hat{z}$-axis is

$$\delta z = \ell\{\cos(\theta + \delta\theta) - \cos(\theta)\}, \tag{A.2}$$

which, for small $\delta\theta$, reduces to

$$\delta z = -\ell \sin\theta \delta\theta. \tag{A.3}$$

**IOP** Institute of Physics ⬤ DEUTSCHE PHYSIKALISCHE GESELLSCHAFT

Using $\delta\alpha = -\delta z/z$, we have

$$\delta\theta = \frac{\delta\alpha}{\tan\theta}. \tag{A.4}$$

Therefore,

$$\delta\langle\cos^2\theta\rangle = -2\langle\cos^2\theta\rangle\delta\alpha, \tag{A.5}$$

which can be rewritten in the following form:

$$\frac{\partial\ln\langle\cos^2\theta\rangle}{\partial\alpha} = -2. \tag{A.6}$$

Integrating equation (A.6), we obtain

$$\langle\cos^2\theta\rangle = \tfrac{1}{3}e^{-2\alpha}, \tag{A.7}$$

where the factor 1/3 is the integration constant so that at zero compression, when $\alpha = 0$, $\langle\cos^2\theta\rangle = 1/3$ in the isotropic case. Substituting equation (A.1) for $\alpha$ and $L_{\min} = L - \Delta L$ in equation (A.7) leads to equation (13):

$$\langle\cos^2\theta\rangle = \frac{1}{3}\left(1 - \frac{\Delta L}{L}\right)^2. \tag{A.8}$$

## References

[1] Kistler S S 1931 *Nature* **127** 741
[2] Tillotson T M and Hrubesh L W 1992 *J. Non-Cryst. Solids* **145** 44
[3] Zimmermann A, Gross J and Fricke J 1995 *J. Non-Cryst. Solids* **186** 238
[4] Akimov Yu K 2003 *Instrum. Exp. Tech.* **46** 287
[5] Burchell M J, Graham G and Kearsley A 2006 *Annu. Rev. Earth Planet. Sci.* **34** 385
[6] Poelz G and Rietmueller R 2006 *Nucl. Instrum. Methods* **34** 491
[7] Reim M, Korner W, Manara J, Korder S, Arduini-Schuster M, Ebert H P and Fricke J 2005 *Sol. Energy* **79** 131
[8] Bellini T, Clark N A and Schaefer D W 1995 *Phys. Rev. Lett.* **74** 2704
[9] Chan M H W, Blum K I, Murphy S Q, Wong G K S and Reppy J D 1988 *Phys. Rev. Lett.* **61** 1950
[10] Porto J V and Parpia J M 1998 *Phys. Rev.* B **59** 14583
[11] Halperin W P, Choi H, Davis J P and Pollanen J 2009 *J. Phys. Soc. Japan* **77** 111002
[12] Kim S B, Ma J and Chan M H W 1993 *Phys. Rev. Lett.* **71** 2268
[13] Volovik G E 1996 *J. Exp. Theor. Phys. Lett.* **63** 301
[14] Fomin I 2004 *J. Exp. Theor. Phys.* **98** 974
[15] Aoyama K and Ikeda R 2005 *Phys. Rev.* B **72** 012515
[16] Vicente C L, Choi H C, Xia J S, Halperin W P, Mulders N and Lee Y 2005 *Phys. Rev.* B **72** 094519
[17] Pollanen J, Shirer K R, Blinstein S, Davis J P, Choi H, Lippman T M, Halperin W P and Lurio L B 2008 *J. Non-Cryst. Solids* **354** 4668
[18] Bhupathi P, Hwang J, Martin R M, Blankstein J, Jaworski L, Mulders N, Tanner D B and Lee Y 2009 *Opt. Express* **17** 10599
[19] Born M and Wolf E 1999 *Principles of Optics* 7th edn (Cambridge: Cambridge University Press)
[20] Wu S T, Efron U and Hess L D 1984 *Appl. Phys. Lett.* **44** 1033
[21] Escuti M J, Cairns D R and Crawford G P 2004 *J. Appl. Phys.* **95** 2386
[22] Gross J, Fricke J, Pekala R W and Hrubesh L W 1992 *Phys. Rev.* B **45** 12774
[23] Gross J, Reichenauer G and Fricke J 1988 *J. Phys. D: Appl. Phys.* **21** 1447

[24] Scherer G W, Smith D M, Qiu X and Anderson J M 1995 *J. Non-Cryst. Solids* **186** 316

[25] Smith D M, Scherer G W and Anderson J M 1995 *J. Non-Cryst. Solids* **188** 191

[26] Herman T, Day J and Beamish J 2006 *Phys. Rev.* B **73** 094127

[27] Venkateswara Rao A 1998 *J. Mater. Synth. Process.* **6** 37

[28] Malitson I H 1965 *J. Opt. Soc. Am.* **55** 1205

[29] Sutton L E and Stavroudis O N 1961 *J. Opt. Soc. Am.* **51** 901

[30] Simanek E 1977 *Phys. Rev. Lett.* **38** 1161

[31] Carr G L, Pekowitz S and Tanner D B 1985 *Infrared and Millimeter Waves* vol 13, V ed K J Button (Orlando, FL: Academic) pp 171–263

[32] Buzykaev A R, Danilyuk A F, Ganzhur S F, Kravchenko E A and Onuchin A P 1999 *Nucl. Instrum. Methods* **433** 396

[33] Kunzner N, Diener J, Gross E, Kovalev D, Timoshenko V Yu and Fujii A M 2005 *Phys. Rev.* B **71** 195304

[34] Golovan L A, Kashkarov P K and Timoshenko V Yu 2007 *Crystall. Rep.* **52** 672

[35] Stratton J A 1941 *Electromagnetic Theory* (New York: McGraw-Hill)

[36] Osborn J A 1945 *Phys. Rev.* **67** 351

[37] Ward I M 1985 *Structure and Properties of Oriented Polymers* (London: Applied Science Publishers)

[38] Schaefer D W and Keefer K D 1986 *Phys. Rev. Lett.* **19** 2199

[39] Emmerling A and Fricke J 1997 *J. Sol–Gel Sci. Technol.* **8** 781

[40] Ma H-S, Prévost J-H and Scherer G W 2002 *Int. J. Solids Struct.* **39** 4605